AFRL-AFOSR-VA-TR-2023-0356

Multifunctional dielectric metasurface for coding/decoding and sensing of light

Brongersma, Mark
LELAND STANFORD JUNIOR UNIVERSITY
450 SERRA MALL
STANFORD, CA,
US

05/16/2023
Final Technical Report

DISTRIBUTION A: Distribution approved for public release.

Air Force Research Laboratory
Air Force Office of Scientific Research
Arlington, Virginia 22203
Air Force Materiel Command

REPORT DOCUMENTATION PAGE

PLEASE DO NOT RETURN YOUR FORM TO THE ABOVE ORGANIZATION.

1. REPORT DATE	2. REPORT TYPE	3. DATES COVERED	
20230516	Final	START DATE 20180515	END DATE 20210514

4. TITLE AND SUBTITLE
Multifunctional dielectric metasurface for coding/decoding and sensing of light

5a. CONTRACT NUMBER	5b. GRANT NUMBER	5c. PROGRAM ELEMENT NUMBER
	FA9550-18-1-0323	61102F
5d. PROJECT NUMBER	**5e. TASK NUMBER**	**5f. WORK UNIT NUMBER**

6. AUTHOR(S)
Mark Brongersma

7. PERFORMING ORGANIZATION NAME(S) AND ADDRESS(ES)
LELAND STANFORD JUNIOR UNIVERSITY
450 SERRA MALL
STANFORD, CA
US

8. PERFORMING ORGANIZATION REPORT NUMBER

9. SPONSORING/MONITORING AGENCY NAME(S) AND ADDRESS(ES)	10. SPONSOR/MONITOR'S ACRONYM(S)	11. SPONSOR/MONITOR'S REPORT NUMBER(S)
Air Force Office of Scientific Research 875 N. Randolph St. Room 3112 Arlington, VA 22203	AFRL/AFOSR RTB1	AFRL-AFOSR-VA-TR-2023-0356

12. DISTRIBUTION/AVAILABILITY STATEMENT
A Distribution Unlimited: PB Public Release

13. SUPPLEMENTARY NOTES

14. ABSTRACT
Photonic metasurfaces are metamaterials with a reduced dimensionality and are comprised of engineered subwavelength-scale meta-atoms. These flat optical elements facilitate a wide variety of custom-tailored electromagnetic responses. They have gained notable attention for their ability to (in certain cases) replace bulky optical elements, such as lenses, prisms, etc., and to allow for dynamic functions, such as optical beamsteering. In this program, we aimed to design metasurfaces for coding/decoding and sensing of the fundamental properties of light (frequency, polarization, direction, intensity,..). Metasurfaces have been particularly useful for this purpose as their diffraction behavior is very sensitively dependent on the properties of light waves. For example, they have successfully been used to perform spectropolarimetry by decomposing plane waves into a set of separated beams that each carry information on the incident angle, spectral content and polarization state. However, such metasurfaces need to be used in conjunction with a separate image sensor to create a complete spectro-polarimetric system. To allow further device integration, it is critical to explore whether the spectral/polarization decomposition and the photodetection processes can be combined in a single metasurface. This has been particularly hard for the detection of circularly polarized light (CPL). Such waves are comprised of two orthogonally-polarized light waves for which the electric fields are oscillating with a ???? phase shift and this relative phase information is lost in the photodetection process. As a result, CPL detection typically involves the use of a quarter-wave plate and linear polarizer on top of a (non-chiral) photodetector. It is however well worth exploring new ways to measure the properties of CPL given its increasingly prominent role in many applications including quantum optics and communication, drug design and development, remote sensing and spectropolarimetry, imaging, valley optoelectronics, and topological photonics. For this reason, we have design and constructed photodetectors that operate at the fundamental limit of CPL photodetection. Along the way, we have also devoted efforts to better understand the optical interaction between metasurface building blocks and to the creation of dynamically-tunable building blocks for metasurfaces.

15. SUBJECT TERMS

16. SECURITY CLASSIFICATION OF:			17. LIMITATION OF ABSTRACT	18. NUMBER OF PAGES
a. REPORT	b. ABSTRACT	c. THIS PAGE		
U	U	U	UU	25

19a. NAME OF RESPONSIBLE PERSON	19b. PHONE NUMBER *(Include area code)*
ARJE NACHMAN	426-8427

Standard Form 298 (Rev.5/2020)
Prescribed by ANSI Std. Z39.18

DISTRIBUTION A: Distribution approved for public release.

Performance Report

Multifunctional dielectric metasurface for coding/decoding and sensing of light

AFOSR Grant Number FA9550-18-1-0323
05/15/2017 to 05/14/2020

Grantee Institution: **Stanford University**
476 Lomita Mall
Stanford, CA 94305

Program Manager: **Dr. Arje Nachman, CIV USAF AFMC AFOSR/RTB**
Tel: 703-696-8427
Email:arje.nachman@us.af.mil

Principal Investigator: **Dr. Mark L. Brongersma**
Tel: (650) 736 2152
Email: Brongersma@stanford.edu

DISTRIBUTION A: Distribution approved for public release.

Table of Contents

DISTRIBUTION A: Distribution approved for public release.

I. Executive summary

I.1. Statement of objectives and key accomplishments

Photonic metasurfaces are metamaterials with a reduced dimensionality and are comprised of engineered subwavelength-scale meta-atoms. These flat optical elements facilitate a wide variety of custom-tailored electromagnetic responses. They have gained notable attention for their ability to (in certain cases) replace bulky optical elements, such as lenses, prisms, etc., and to allow for dynamic functions, such as optical beamsteering. In this program, we aimed to design metasurfaces for coding/decoding and sensing of the fundamental properties of light (frequency, polarization, direction, intensity,..). Metasurfaces have been particularly useful for this purpose as their diffraction behavior is very sensitively dependent on the properties of light waves. For example, they have successfully been used to perform spectropolarimetry by decomposing plane waves into a set of separated beams that each carry information on the incident angle, spectral content and polarization state. However, such metasurfaces need to be used in conjunction with a separate image sensor to create a complete spectro-polarimetric system. To allow further device integration, it is critical to explore whether the spectral/polarization decomposition and the photodetection processes can be combined in a single metasurface. This has been particularly hard for the detection of circularly polarized light (CPL). Such waves are comprised of two orthogonally-polarized light waves for which the electric fields are oscillating with a $\pm\pi/2$ phase shift and this relative phase information is lost in the photodetection process. As a result, CPL detection typically involves the use of a quarter-wave plate and linear polarizer on top of a (non-chiral) photodetector. It is however well worth exploring new ways to measure the properties of CPL given its increasingly prominent role in many applications including quantum optics and communication, drug design and development, remote sensing and spectropolarimetry, imaging, valley optoelectronics, and topological photonics. For this reason, we have design and constructed photodetectors that operate at the fundamental limit of CPL photodetection. Along the way, we have also devoted efforts to better understand the optical interaction between metasurface building blocks and to the creation of dynamically-tunable building blocks for metasurfaces.

The successful realization of our research objectives is expected to provide a new platform and new set of tools for developing ultrathin, planar optical elements for sophisticated sensing and coding/decoding functions. The ability to encode, decode and measure the fundamental properties of light may find applications in military target acquisition and identification, chemical inspection, multispectral-channel combination, communication, laser technology and quantum information processing.

DISTRIBUTION A: Distribution approved for public release.

II. Research Accomplishments

II.1. The emergent optical properties of nanostructure pairs and arrays

The overarching goal of this research program is to develop dielectric metasurfaces for coding/decoding and sensing of light. These flat optical elements are constructed from high-index nanostructures, also known as optical antennas, that can strongly scatter light in an engineerable fashion[2–4]. Optical resonances play a critical role in the design of optical antennas as they control the strength and nature of the scattering process. An enormous body of research has been devoted to explore how the resonant properties of individual metallic and semiconductor nanostructures can be tailored, but less is known about the ways in which resonances are modified when they are placed into a dense array. The resonances of nanostructures can significantly evolve in their character and move in spectral location as nano particles are brought into close proximity. In our work, we aimed to elucidate the emergent optical properties of pairs and small clusters. In these systems, the changes in scattering behavior can result from the non-trivial electromagnetic interactions of nanoresonators. Conventionally, an equivalent chemical bonding model[5–7] is used to describe the optical coupling between nanoresonators and the associated structural colors. Under a quasi-electrostatic approximation, only bonding and anti-bonding modes can be formed in a pair system through modal hybridization. Significant shifts of the resonance frequency (or splitting thereof) is only expected when the optical near fields strongly overlap (i.e., two nanostructures are extremely close to each other). However, studies on the scattering properties of metallic nanoparticle pairs/arrays[8] suggest that, besides the radiative decay of plasmon resonances, the spectral shape of the scattered light can also be modulated even in the absence of near-field coupling. Although the spectral shifts are found to be small for 0D nanoparticle pairs due to the inefficient radiative coupling, these results indicate the possibility of realizing structural color if a strong radiative coupling can be achieved between two nanoresonators. Radiative coupling has also proven to be important in coupled silicon (Si) NW systems and facilitated the creation of angle-sensitive detection systems[9].

In our research, we demonstrate both theoretically and experimentally that Si NW pairs can display structural colors across the entire visible spectral range by controlling their radiative coupling. A series of additional Fabry-Pérot-type modes can be formed as a consequence of iterative light scattering between two neighboring NWs. These quasinormal modes (QNMs)[10] cannot be predicted by the conventional chemical hybridization model, which exhibits/predicts only bonding and anti-bonding modes. Instead, a nonlinear frequency-dependent Green's function must be used to describe the coupling between two neighboring NWs. The resonant frequency of the fundamental Fabry-Pérot mode is strongly shifted with respect to the original resonant frequency of a single NW, even in the absence of evanescent-field coupling. The resonant frequency can be tuned controllably across the entire visible frequency range by changing the distance between the two NWs while preserving significant color purity. Therefore, a NW pair with fixed NW dimensions can function as a universal building block for structural color, while maintaining a sub-wavelength footprint.

We start our analysis by considering an individual square cross-sectional Si NW, which supports a range of leaky Mie-type optical resonances. By performing a QNM analysis of the scattering spectrum of the NW, we find that its optical response is dominated by the fundamental TM_{11} QNM. As shown in the inset of Fig. 1(b), the TM_{11} mode bears an electric field distribution with one antinode in the $\tilde{E}_z$-field (parallel to the NW) distribution inside the NW, indicating that it behaves as a resonant electric dipole. The linear electric dipole moment is given by $p_z = \alpha E_{z,\mathrm{inc}}$, where α denotes the polarizability and $E_{z,\mathrm{inc}}$ the incident field at the center of the NW. We further assume that the polarizability α takes the following simple form:

DISTRIBUTION A: Distribution approved for public release.

$$\alpha = \frac{-i\kappa}{\tilde{\omega}_0 - \omega}\,, \tag{1}$$

where $\tilde{\omega}_0 = \omega_0 - i\gamma_0$ is the complex frequency of the TM_{11} QNM and κ a complex frequency-independent coefficient. We note that this single-pole formula is only approximative. It neglects the embodiment of higher-order multipoles, which are not fully negligible according to the QNM analysis. Its main strength is its simplicity and accuracy to quantitatively model the NW polarizability in the spectral range of interest. We retrieve $\tilde{\omega}_0$ from QNM computation using the mode solver of COMSOL valid for non-dispersive materials dispersion, and κ is obtained by fitting Eq. (1) with full-field simulation results α_{sim} of the polarizability obtained by integrating the local polarizability over the NW cross section, $\alpha_{\mathrm{sim}} = \int \varepsilon_0(\varepsilon_{\mathrm{Si}} - 1)E_{\mathrm{z}}(\mathbf{r})dS/E_{\mathrm{z,inc}}(\mathbf{r} = 0)$. Here, $E_{\mathrm{z}}(\mathbf{r})$ is the electric-field distribution of the NW under plane-wave illumination ($\mathbf{r} = 0$ is the center of the Si NW) and $\varepsilon_{\mathrm{Si}} = 16$ is the relative permittivity of Si. The good agreement between α_{sim} and the fitted polarizability α, clearly indicates that Eq. (1) is a reasonable approximation.

Next, we focus on a Si NW pair system as shown in Fig. 1(a). We apply the coupled dipole theory [50,51] in order to simply take the interaction between NWs (effective linear dipoles p_1 and p_2) into account:

$$\begin{pmatrix} i(\tilde{\omega}_0 - \tilde{\omega}) & -\kappa G(d, \tilde{\omega}) \\ -\kappa G(d, \tilde{\omega}) & i(\tilde{\omega}_0 - \tilde{\omega}) \end{pmatrix} \begin{pmatrix} p_1 \\ p_2 \end{pmatrix} = 0. \tag{2}$$

The diagonal terms correspond to the intrinsic harmonic oscillation of the individual linear dipoles, where $\tilde{\omega}$ is the complex eigen frequency of the system, and the off-diagonal terms represent the coupling between the two linear dipoles. $G(d, \tilde{\omega}) = \frac{ik^2}{4\varepsilon_0} H_0(kd)$ is the Green's function that defines the scattered field in terms of the dipole moment. H_0 is the zeroth-order Hankel function, d is the distance between the two effective dipoles, and $k = \frac{\tilde{\omega}}{c}$ is the complex eigen wave vector for the coupled NWs. We emphasize that the off-diagonal term (i.e., the coupling strength) $g(\tilde{\omega}) = \kappa G(d, \tilde{\omega})$ does not linearly depend on frequency. As a result, the determinant of the 2×2 matrix $\det(A(\omega)) = 0$ – which is used to find the eigenvalues (or poles) of the coupled NW system – is no longer simply the common quadratic polynomial in one variable $\tilde{\omega}$. The number of solutions is therefore no longer restricted to two.

DISTRIBUTION A: Distribution approved for public release.

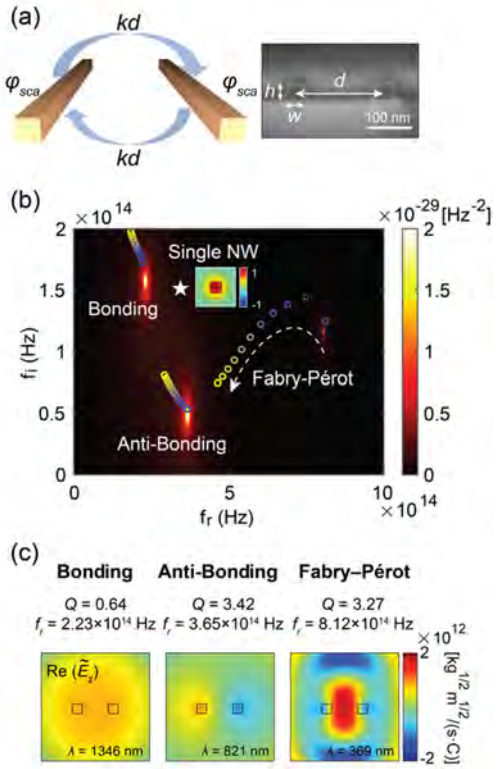

Fig. 1. Fabry-Pérot mode in a Si NW pair. (a) Left: the QNM is formed as the result of light scattering back and forth between two neighboring NWs. Right inset: cross-section scanning electron microscope (SEM) image of the fabricated Si NW pair. (b) Calculated reciprocal $1/\det(A(\tilde{\omega}))$ of the determinant of the 2×2 matrix used to model the coupled NW (dipole) system as a function of the real and imaginary parts of complex frequency $\tilde{\omega}$. The NW separation distance is 200 nm. The QNM frequencies computed with QNMEig for the bonding, anti-bonding and Fabry-Pérot modes are overlaid as a function of the NW spacing from 200 nm (blue circles) to 400 nm (yellow circles) in steps of 20 nm. The $\tilde{E}_z$-field distribution of the dipolar TM_{11} QNM for single NW (located at the white star position) is also plotted for reference. (c) Out-of-plane electric-field distributions $\tilde{E}_z(x,y)$ of the three simulated QNMs for a 200-nm spacing. In all plots, the modes are normalized with the PML-normalization method [53]. The normalization allows for a direct visual comparison of the interaction strength of the mode with driving field. All data are obtained for a 50-nm square size NW and for a Si permittivity $\varepsilon_{Si} = 16$.

The above analysis is in sharp contrast with most of the reported chemical bonding models used to describe the coupling between two optical resonators, in which the off-diagonal term is usually assumed to be independent of frequency for a given system, and governed by the near-field overlap of the two resonators. We emphasize that such a fixed-coupling-strength approximation is only valid if the coupling strength g is much smaller than the original complex frequency $\tilde{\omega}_0$. This is generally well-applicable for high-Q resonators for which the evanescent fields vanish very quickly away from the resonator surface. As a result, the mode splitting is relatively weak ($\tilde{\omega} \sim \tilde{\omega}_0$) and thus $g(\tilde{\omega})$ can be reasonably approximated by $g(\tilde{\omega}_0)$. However, this approximation fails for highly leaky optical resonators such as the fundamental TM_{11} Mie modes for Si NWs where $Q \sim 1$. The radiative fields of these low-Q leaky modes have a natural phase evolution and grow exponentially in amplitude with the distance away from the resonator in the QNM profile. This originates from the exponential decay of the amplitude of the mode in time domain. Therefore, the coupling strength g oscillates with increasing NW distance and can be comparable to the original frequency ω_0, resulting in a non-negligible difference between $g(\tilde{\omega})$ and $g(\tilde{\omega}_0)$.

DISTRIBUTION A: Distribution approved for public release.

To show this, we apply the above coupled dipole theory to a 50-nm sized square Si (refractive index n = 4) NW pair with 200-nm center-to-center distance. The retrieved effective linear dipole polarizability for single NW is $\frac{-i\kappa}{\tilde{\omega}_0-\omega} = \frac{(6.1-5.2i)\times10^{-11}}{(3.4-1.5i)\times10^{14}-f}$ $[F\cdot m]$. The reciprocal of the determinant of the 2×2 matrix $abs(\frac{1}{-(\tilde{\omega}_0-\tilde{\omega})^2-\kappa^2G^2(d,\tilde{\omega})})$ is plotted in the complex frequency plane as shown in Fig. 1(b), such that the QNM frequencies occur as pole maxima. Three poles can be found within the frequency range of interest, indicating that there are at least three QNMs for the studied NW pair system. In order to verify the existence of the QNMs predicted with the dipole approximation, we perform full wave simulations with the mode solver of COMSOL. We overlay the complex frequencies found from QNM simulations for a NW distance ranging from 200 nm (blue circles) to 400 nm (yellow circles) in steps on 20 nm, to track the modal dispersion. The complex frequency of the TM_{11} QNM for a single NW (white star) is also shown for reference. We attribute the small difference between the frequencies obtained from the analytical poles and blue circles to the imprecise nature of Eq. (1). Figure 1(c) shows the out-of-plane electric field distribution of the three eigen modes as retrieved with the numerical solver. We find that the first two of the three modes can be recognized as the conventional bonding (lower frequency) and anti-bonding (higher frequency) modes, mimicking the chemical bonding model. It should be noted that both show a red shift with increasing NW spacings and do not converge to the complex frequency of the original TM_{11} QNM for large d. This highlights the oscillating and frequency-dependent nature of the dipole-dipole coupling strength.

The third QNM on the other hand, which exhibits an antinode in the air gap between the two NWs, is rather unique and is not predicted from the conventional chemical bonding model. The complex frequency of this mode shifts significantly from that of the original TM_{11} mode (single NW), revealing a considerable coupling strength between the neighboring NWs. We attribute the formation of this mode to a Fabry-Pérot resonance between two NWs, where light is iteratively scattered back and forth between the NWs. At resonance, two NWs are in phase as 2π is accumulated when light scattered from one NW to the other. In order to visualize this physical picture, we decompose the phase evolution into two parts: the scattering phase from of the NWs $\varphi_{\text{sca}} = arg(\frac{-i\kappa}{\tilde{\omega}_0-\tilde{\omega}_{\text{FP}}}\tilde{\omega}_{\text{FP}}{}^{3/2}e^{i\frac{\pi}{4}})$ and the propagation phase in the air gap $\varphi_{\text{prop}} = Re\left(\frac{\tilde{\omega}_{\text{FP}}}{c}d\right)$. Figure 2(a) shows the phase decomposition results as a function of the NW separation distance d. We find that a constant 4π phase evolution is observed when the light travels back and forth in one round trip, regardless of d. This evidences the Fabry-Pérot nature of the QNM. Note that higher-order Fabry-Pérot modes can also be found in the studied coupled NW system, as long as $2n\pi$ $(n = 2, 3, \dots)$ phase is accumulated when light bounces back and forth in one roundtrip

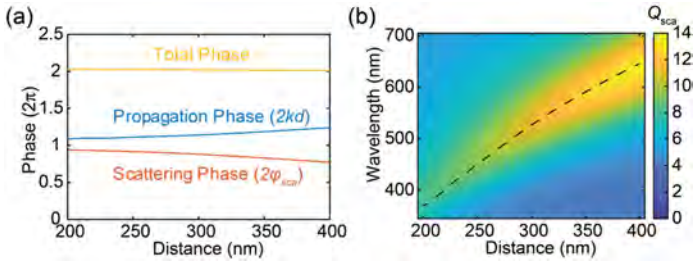

Fig. 2. Fabry-Pérot resonant nature of the new mode found for the Si NW pair. (a) Total phase (yellow), scattering phase (orange), and propagation phase (blue) of the Fabry-Pérot mode as a function of distance between two NWs. The phases are calculated at resonance using complex frequencies from numerical QNM simulation. (b) Simulated scattering efficiency of the Si NW pair as a function of incident wavelength and NW separation distance under normally-incident TM-polarized illumination. The black dashed line represents the center wavelengths of the Fabry-Pérot modes for increasing NW separations as obtained from QNM simulations.

DISTRIBUTION A: Distribution approved for public release.

The Fabry-Pérot QNM shows stronger dispersion with the separation distance (200 nm $< d <$ 400 nm) compared to the bonding and anti-bonding modes as shown in Fig. 1(b). The resonant frequency spans almost the entire visible frequency range from ~4.6×10^{14} Hz to 8.1×10^{14} Hz (corresponding to 370 nm - 650 nm) when the distance between the two NWs varies from 200 nm to 400 nm. As a result, we envision that the demonstrated Fabry-Pérot mode may function as a new type of universal building block to achieve structural color. Each unit cell would be composed of similar-sized nanostructures like photonic crystals, but with a varying NW spacing. Such a design also offers subwavelength resolution similar to resonant particles. Figure 2(b) shows the simulated scattering efficiency of the Si NW pair as a function of the incident wavelength and NW spacing under normally-incident TM polarized illumination. A single scattering peak is observed for every NW spacing. The positions of the peaks perfectly overlap with the real parts of the complex frequencies predicted with the QNM simulations (black dashed curve). This additionally corroborates that the main scattering characteristic of NW pairs originates from the excitation of a Fabry-Pérot mode. We have also used QNM expansion theory to quantitatively verify that the dominant contribution to the scattering cross-section spectrum of the pair is the Fabry-Pérot QNM.

The dispersion of Si has been neglected in the previous analysis, although both the real and imaginary parts of the refractive index of Si appreciably vary in the spectral region of the Fabry-Pérot QNM, for $\lambda <$ 450 nm. To confirm the existence of that mode, we have repeated the QNM computations with a Si permittivity function consisting of pairs of Lorentz poles and using either the QNM solvers QNMEig or the freeware MAN (Modal Analysis of Nanoresonators). We find that the resonant frequency $Re(\tilde{\omega}_{\mathrm{FP}})$ of the Fabry-Pérot mode is only slightly changed by adding dispersion. This can be attributed to the fact that Fabry-Pérot and nanowire resonances, $Re(\tilde{\omega}_{\mathrm{FP}})$ and $Re(\tilde{\omega}_0)$, are significantly different so that the propagation phase φ_{prop} dominantly sets the Fabry-Pérot condition. On the other hand, the quality factor is significantly decreased owing to the large value of $Im(\varepsilon_{\mathrm{Si}})$ at short wavelengths.

Additionally, with the solver QNMEig, we found that there exist a great number of higher-order modes with frequencies close to $Re(\tilde{\omega}_{\mathrm{FP}})$ for small NW spacings ($d <$ 250 nm), for which the fields inside the Si NWs exhibit more than one anti-node. These higher-order modes also exist when the dispersion is turned off, but at frequencies much larger than $Re(\tilde{\omega}_{FP})$. Dispersion pushes them closer to $Re(\tilde{\omega}_{\mathrm{FP}})$ because of the increased refractive index of Si at shorter wavelengths. We also note that some of these higher-order modes are characterized by strong fields in the air region between the two wires. In analogy to the Fabry-Pérot mode mentioned above which is caused by the non-linear coupling between the dipolar modes of the wire, these modes are formed by the radiating coupling between wire multipole modes, and may thus be named multipolar Fabry-Pérot modes. When the resonator is excited by a monochromatic plane wave, both the higher-order modes (whether they are multipolar Fabry-Pérot modes or not) and the Fabry-Pérot mode can be excited, leading to a complicated response spectrum. In the experimental study discussed below, we mostly focus on NW pairs with Fabry-Pérot mode resonance wavelengths larger than 450 nm, and thus ignoring the dispersion of Si makes for a reasonable assumption. Furthermore, the higher-order modes do not play an important role in the scattering response.

To demonstrate the color generation of the Si NW pair experimentally, we fabricate a series of Si NW pairs with varying NW spacing on a sapphire substrate using electron-beam lithography. The fabricated NWs all have a similar square cross-section (Fig. 1a) with dimensions around 50 nm. The length of the NWs is chosen to be 50 μm to avoid finite-length effects [56]. Figure 3(a) shows the bright-field cross-polarized reflection optical image, in which Si NW pairs scatter different colors of light. The observed colors span almost all the way from the blue to red as a function of the NW spacing, confirming the potential of Si NW pairs as building blocks for structural color.

DISTRIBUTION A: Distribution approved for public release.

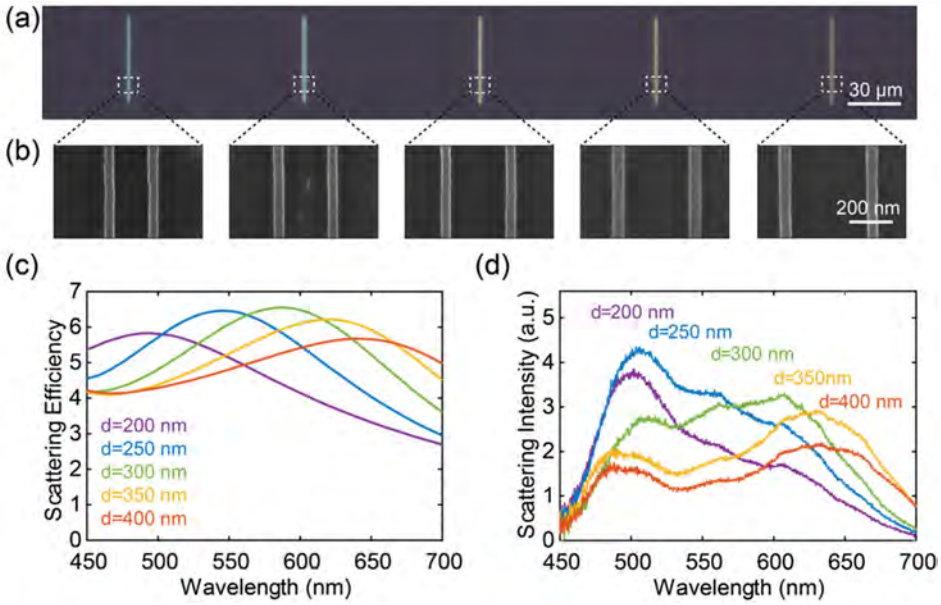

Fig. 3. Experimental demonstration of structural color from Si NW pairs. (a) Cross-polarized reflection optical image of the fabricated Si NW pairs. All the NWs are 50-μm long and have the same 50-nm square size. (b) Top-view scanning electron microscope images of fabricated Si NW pairs. The separation distance between the NWs increases from 200 nm to 400 nm in steps of 50 nm. (c) Simulated scattering efficiency of the designed Si NW pairs on sapphire substrate as a function of the incident wavelength under normally-incident TM-polarized illumination. The dispersion and absorption of Si are considered in the simulation. (d) Measured cross-polarized reflection spectra for the different fabricated Si NW pairs.

The corresponding top-view scanning electron microscope images are shown in Fig. 3(b). We perform full-field simulations for the fabricated structures by taking the material dispersion and asymmetric dielectric environment into account. The simulated scattering efficiency spectra under normally-incident TM polarized illumination are shown in Fig. 3(c). All the NW pairs show a strong, single scattering peak at a resonance wavelength between 490 nm and 650 nm as the distance between the NWs increases from 200 nm to 400 nm. Figure 3(d) shows the measured cross-polarized reflection spectra for different Si NW pairs that were taken using a confocal optical microscope. In order to filter out the direct reflection from the sapphire substrate, the incident beam is firstly polarized 45 degree with respect to the NW direction. Next, the scattered light is collected through a second polarizer, which is oriented orthogonal to the first one. In this cross-polarized measurement scheme, only light scattered by the NWs is collected. In general, the measured reflection spectra are in good agreement with the simulated scattering efficiency spectra. The additional reflection peak around 500 nm may result from the non-uniform transmittance of the second polarizer, and small kinks in the spectra (560 nm, 610 nm, etc.) are caused by the interference in polarizer thin films. A higher scattering peak contrast is observed in the measurements as compared to the simulations in which the scattering to all the angles are included. This is attributed to the fact that the scattering from the excited Fabry-Pérot modes are highly directional normal to the substrate, which lies within the NA = 0.4 of the collection objective used in the measurement. We should note that the demonstrated structural color from the Si NW pairs has a strong polarization and angular dependence, which can be useful in novel applications such as transflective displays and optical information encryption.

DISTRIBUTION A: Distribution approved for public release.

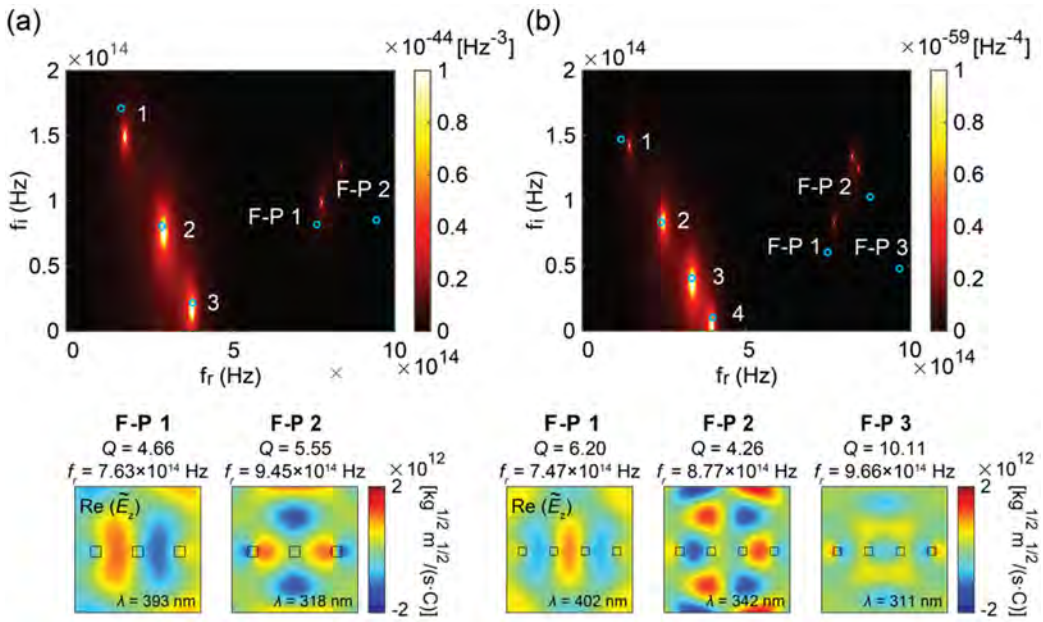

Fig. 4. Fabry-Pérot modes in Si NW arrays. Calculated reciprocal of the determinant of the 3×3 matrix (a) and 4×4 matrix (b) used to describe the resonance modes of linear arrays composed of 3 or 4 NWs in a free space, as a function of the real and imaginary part of their complex frequencies. The NW separation distance is 200 nm. The complex frequencies of the QNMs computed with COMSOL for a constant Si permittivity are overlaid as blue circles. The out-of-plane electric field distributions of the corresponding Fabry-Pérot modes are shown in the lower panel.

Finally, we note that the Fabry-Pérot modes demonstrated above are not only supported by a NW pair, but can also be seen in assemblies comprised of a plurality of NWs. The Fabry-Pérot modes exist universally through the coupling between NWs (linear electric dipoles). The coupled dipole theory for *n* NWs can be generalized as follows:

$$\sum_m A_{l,m}\, p_m = 0 \quad (l, m = 1,2,\cdots,n) \tag{3}$$

where $A_{l,l} = i(\tilde{\omega}_l - \tilde{\omega})$ and $A_{l,m\,(l\neq m)} = -\kappa_l G(d_{l,m}, \tilde{\omega})$. $\tilde{\omega}_l$ and κ_l are the complex eigen frequency and coupling coefficient for the *l*th NW, and $d_{l,m}$ is the distance between the *l*th and *m*th NW. Figure 4 shows the reciprocal of the determinant of the 3×3 matrix and 4×4 matrix used to describe the coupling between three or four identical NWs arranged in parallel in free space, as a function of real and imaginary part of complex frequency. Besides the conventional modes expected from the chemical bonding model (labeled as 1, 2, 3…), multiple Fabry-Pérot modes can also be found in both cases. The number of Fabry-Pérot modes of the same order supported is equal to the number of air gaps in the NW chain. The complex frequencies from numerical QNM simulations are overlaid with blue circles and are in good agreement with the analytical results (poles on the complex plane) under the dipole approximation. The electric field distributions of the simulated QNMs shown in Fig. 4 confirm the Fabry-Pérot resonant nature of these modes: the electric field is concentrated in the space between neighboring wires. These Fabry-Pérot modes resonate at different wavelengths and can be labeled by their quasi in-plane momentum. Therefore, with a change of the incident angle, different Fabry-Pérot modes dominate the excitation, leading to the change of the scattering color. As the number of NWs increases, we move from a regime in which a few discrete QNMs dominate the structural color response to a regime in which the well-known iridescence of periodic structures should take place with a continuum of QNMs indexed by the in-plane momentum wavenumber. The QNM at Γ point for a periodic structure is a one-

DISTRIBUTION A: Distribution approved for public release.

dimensional cavity mode with symmetric radiation profiles with respect to the plane of NW array, and therefore renders the Si NW array at resonance as a perfect semiconductor meta-mirror.

In summary, we demonstrate both theoretically and experimentally that two identical neighboring Si NWs with different spacings form a new universal building block for structural color, while maintaining a sub-wavelength footprint. The structural color results from a series of Fabry-Pérot modes formed by light that is bouncing back and forth between two NW nanoresonators, and can be tuned across the entire visible spectrum by varying the inter-wire distance. These Fabry-Pérot modes are not expected from the conventional chemical bonding model. Instead, they can be well described by considering a nonlinear, frequency-dependent coupling between two NWs. The studied system presents a novel way to generate optical resonances in coupled nanostructures and expands the understanding of resonant coupling and the manipulation of light with metasurfaces comprised of dense arrays of nanostructures. This work was published in the journal Optica[11].

II.2. Dynamic tuning of optical resonances and modulation of light scattering

In a number of applications, it is of value to dynamically tune optical resonances and modulate the scattering from optical antennas. Nanomechanical systems have an outstanding potential for ultra-low power modulation of optical systems. Under this program, we designed and implemented a nano-electromechanical system (NEMS) to dynamically modulate the gap of a plasmonic dimer at the ultimate, atomic scale (~1 nm), which allows operation at fundamentally-limited optical sensitivities and achievement of low-power (~1 fJ/bit), high-speed (~10 MHz) manipulation of optical signals[12]. To aid the design and verify the operation of this modulator, they capitalized on recent advances in electron energy loss spectroscopy (EELS). This technique measures the energy loss probability of swift electrons as they interact with materials and structures. They employed it follow the modal hybridization of a single, dimer element upon electromechanical actuation inside a transmission electron microscope (TEM) as shown in Fig. 5. Figure 5, a,b show schematic and transmission electron microscopy images of a NEMS that can dynamically tune the gap of a gold (Au) nanoparticle-dimer. The device was fashioned inside a thin Si_3N_4 TEM window. The side-by-side arrangement of the particles allows convenient monitoring of the spatial and spectral properties of the plasmonic modes at different gap sizes. Simulations of EELS spectra (Figure 5,c,d) for this structure illustrate how the interparticle coupling evolves with decreasing gap size. The EELS simulations are performed with the Metallic NanoParticles Boundary Element Method (MNPBEM) toolbox for MATLAB, which solves Maxwell's equations in the presence of an electron beam (see Methods for details). The fundamental dipolar modes of the individual nanoparticles couple to form two new eigenmodes with different modal symmetry: the bonding dipole (BDP) and the anti-bonding dipole (ADP) mode. For gap sizes below 10 nm, the interparticle coupling is sufficiently strong to spectrally separate the two modes. The BDP mode continues to red-shift, ultimately at astounding rates over 100 meV for each nanometer of movement. Based on their different modal symmetries, the BDP and ADP are most effectively excited and probed in different spatial locations. This can be seen in the simulated EELS maps for these modes of a fabricated dimer (Fig.5e) in the strong coupling regime (Fig. 5f). This facilitates modal identification in experiments. The extreme sensitive to the optical modes and resonances to the gap distance was leveraged to realize modulator devices. This work was published in Nature Communications.[13] We also wrote a review article for the journal Science on the topic of dynamic optical wavefront control.[14]

DISTRIBUTION A: Distribution approved for public release.

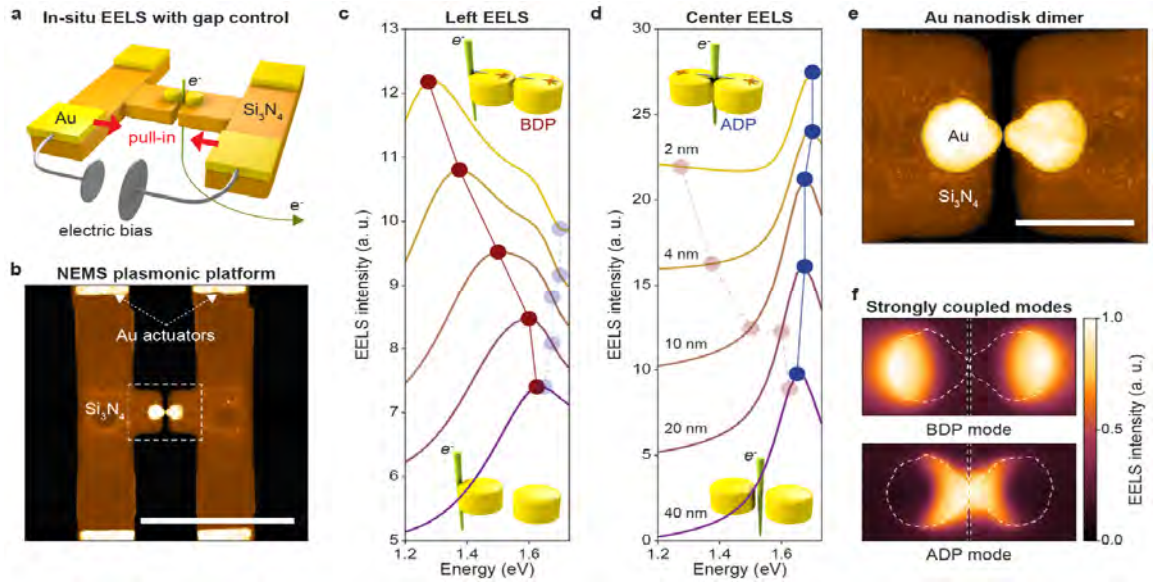

Figure 5. Nanoelectromechanical system (NEMS) with a plasmonic dimer. a, Schematic of the device showing how an external DC bias applied to Au actuators can electrostatically pull two Si_3N_4 beams together and reduce the spacing between two Au nanoparticles. b, False-colored STEM image of the fabricated dimer (white/yellow) and cantilevers (brown). White, dashed rectangle indicates the location of the dimer. Scale bar: 1 μm. (c,d), Simulated EELS spectra as a function of gap size for the electron beam incident on the left edge (c) and the center (d) of gold nanodisk dimer. We apply an increasing 1 step (5 step) offset values to each of the left (center) EELS intensity spectra for improved visibility. The red and blue symbols indicate the location of BDP and ADP modes, respectively. e, Magnified false-colored STEM image of gold nanodisk dimer. The diameter and thickness of gold nanodisk are designed to be 100 nm and 50 nm, respectively. Scale bar: 200 nm. f, Simulated EELS spatial profile of BDP and ADP modes for the gap size of 2 nm. White dashed contour extracted from STEM image (Fig. 1e) has been taken into account in the EELS simulation.

II.3. A nonlocal metasurface for circularly polarized light detection

One of the key goals of this program was to sort light based on its intrinsic properties and sensing these properties directly. Light exhibits distinct interactions with materials that can depend on the intensity, wavelength, incident direction, and polarization state. In nanostructures we can harness plasmonic and Mie resonances to further tailor the ways in which light interacts with matter. Whereas such resonant structures have primarily been exploited to control the flow of light, they can also be employed to uncover the nature of the light that is incident from an optical scene. Dense, planar arrays of nanostructures termed metasurfaces have been particularly useful for this purpose as their diffraction behavior is very sensitively dependent on the properties of light waves. For example, they have successfully been used to perform spectropolarimetry by decomposing plane waves into a set of separated beams that each carry information on the incident angle, spectral content and polarization state[15–22]. However, such metasurfaces need to be used in conjunction with a separate image sensor to create a complete spectro-polarimetric system. To allow further device integration, it is critical to explore whether the spectral/polarization decomposition and the photodetection processes can be combined in a single metasurface. Recently, semiconductor nanowire (NW) arrays have already been incorporated in multispectral detection and imaging systems[23,24]. To gain the maximum possible information from a data stream or optical scene, we need to also determine the state of polarization through a measurement of the Stokes parameters[25]. Using anisotropic semiconductor NWs[26] or metallic slits[27] in the photodetection, it is straightforward to distinguish linear states of polarization. However, the optical detection of

DISTRIBUTION A: Distribution approved for public release.

circularly polarized light (CPL) is inherently more challenging. Such waves are comprised of two orthogonally-polarized light waves for which the electric fields are oscillating with a $\pm\pi/2$ phase shift and this relative phase information is lost in the photodetection process. As a result, CPL detection typically involves the use of a quarter-wave plate and linear polarizer on top of a (non-chiral) photodetector. In fact, many invertebrates such as mantis shrimp, cuttlefish, bees and crickets have developed such compound elements to create CPL-sensitive detection systems for communication and visual contrast enhancement[28]. It is however well worth exploring new ways to measure the properties of CPL given its increasingly prominent role in many applications including quantum optics[29] and communication[30], drug design and development[31], remote sensing[32] and spectropolarimetry[33], imaging[34], valley optoelectronics[35], and topological photonics[36]. Recent pioneering approaches include detectors that employ chiral organic molecules and semiconductors[37–39] and chiral plasmonic structures[40,41]. Plasmonic structures can show particularly high circular dichroism (CD), i.e. differential absorption for left- and right-handed CPL[41–44], but metals tend to make poor photodetectors that can only rely on inefficient hot electron emission. To boost the responsivity, it is highly desirable to explore whether chiral detectors can be made from high electrical-performance, inorganic, achiral semiconductors. Here, we show that a dislocated silicon nanowire (Si NW) metasurface can effectively detect and distinguish left- and right-handed CPL without the need of external filters or waveplates.

Figure 6a shows a conceptual schematic of our proposed CD photodetector. It features a dense array of custom-designed Si NWs on a transparent substrate. The unique shape of the NWs with a periodic array of kinks is engineered to facilitate excitation of a nonlocal guided-mode resonance by normally-incident CPL with one selected handedness while transmitting light waves of the opposite handedness. This enables substantial optical absorption and photocarrier generation in the semiconductor material selectively for the circular polarization (CP) of interest. The polarization can therefore be determined through a measurement of the photocurrent upon application of a small bias voltage to the electrodes. A scanning electron micrograph (SEM) of an array fabricated by electron beam lithography is shown in Fig. 6b.

Before we provide a detailed mechanistic picture of the metasurface operation, we evaluate the fundamental performance limit for this type of device using coupled-mode theory[45,46]. Because of its 2-dimensional nature, the detector can be treated as a single-mode optical resonator in a symmetric external environment. The incident CPL can follow a direct transmission pathway and a resonant pathway through the nanopatterned semiconductor layer (Fig. 6c). When the light follows the resonant pathway and the guided resonance is excited, it leads to a significantly increased energy storage and light absorption. To maximize the CD, we would ideally construct a situation where the incident light can only excite the resonance when its polarization matches the desired handedness. In our example, this will be right-handed circular polarization (RCP). To achieve the strongest possible light absorption, a fraction of the in-coupled light needs to couple back out into free space in order to effectively cancel out the directly transmitted light through destructive interference. The reciprocal nature of this device enforces that on-resonance the out-coupled light from the resonator changes its handedness in the transmission direction. As a result, we see that left-handed circular polarization (LCP) emerges given an RCP incident beam. In order for the directly transmitted light to interfere destructively with the out-coupled light, its polarization should thus also have the opposite handedness and incur a π phase delay with respect to the resonant pathway. In other words, it is essential that the slab serves as a half-wave plate for the direct transmission channel. This is a key insight of our analysis as it provides valuable intuition about possible device designs. Analogous to optical absorption in an ultrathin and freely-suspended metallic film[47], the theoretical limit for the absorptance of RCP light is 0.5 at critical coupling when both the total transmittance and reflectance are 0.25.

DISTRIBUTION A: Distribution approved for public release.

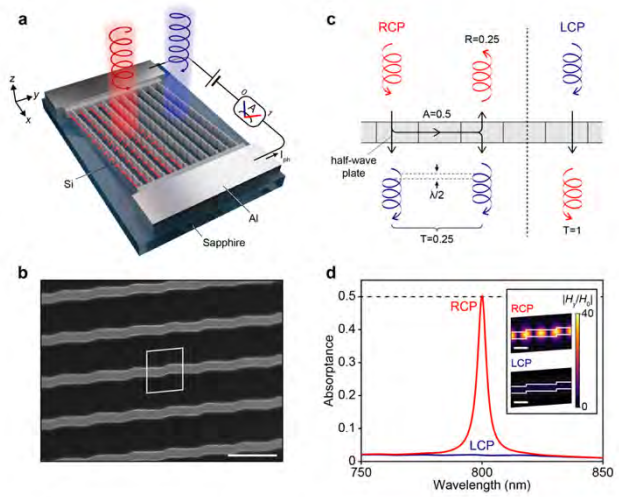

Fig. 6. Dislocated high-index semiconductor metasurfaces for CD. a, Schematic of a CD photodetector using dislocated high-index semiconductor metasurfaces. A dislocated Si NW metasurface displays resonant absorption for a CP of interest (RCP, red) while transmitting the other (LCP, blue), allowing electrical read-out of an incident CP. b, SEM of fabricated Si nanostructures. A unit cell of the periodic structures is outlined by the white box. Scale bar, 500 nm. c, Illustration of an optically resonant nanopatterned semiconductor layer in free space interacting with incident RCP (left) and LCP (right) at critical coupling. d, Simulated optical absorption spectra of a dislocated Si NW metasurface suspended in free space for RCP (red) and LCP (blue). The Si metasurface is designed to present resonant absorption for RCP at λ = 800 nm. The theoretical limit of absorptance is indicated by the black dashed line. Inset: Normalized magnetic field distributions (λ = 800 nm) in the median plane of two adjacent unit cells for RCP (top) and LCP (bottom). Scale bar 200 nm.

Leveraging the insights derived from coupled-mode theory, we aim to identify a nanostructure design for the suspended silicon (Si) film that can both serve as a half-wave plate for the direct transmission pathway and only exhibit an optical resonance for RCP light. Figure 6d shows the optical absorption behavior of our successfully optimized design as obtained by finite-element simulations. As desired, the spectrum for LCP illumination shows a low and relatively constant absorptance across the wavelength range of interest. This results from the non-resonant absorption channel where light is directly transmitted through the film with little dissipation in the Si. On the other hand, the absorption spectrum for RCP light displays a spectrally-narrow resonance with a high optical quality-factor, $Q = 180$. The metasurface achieves critical coupling and the absorptance on resonance is just above the theoretically predicted limit; The slightly larger absorption results from the small amount of non-resonant absorption in the finite-thickness film. The magnetic field distribution in the nanostructured layer on and off resonance are shown as insets. For RCP, the high-Q resonance gives rise to a strong field enhancement inside the NWs. This enables significant optical absorption in the Si despite its weak materials absorption. In the following, we will discuss the intuitive design for the NWs and the physics behind the operation of our CPL detector.

In the design of our metasurface-based photodetector, we aim to use high electronic-performance semiconductors and avoid the use of complex and hard-to-integrate three-dimensional chiral systems, such as arrays of helices[42] and twisted optical metamaterials[43,48,49]. Fortuitously, it has been shown that strong CD can also be obtained in planar chiral metasurfaces[41,50,51], i.e. metasurfaces that are distinguishable from their mirror images (enantiomers) with respect to a line in the plane of the structure. We start the design of our planar chiral metasurface by considering the optical properties of a dense, subwavelength array of straight Si NWs. Such anisotropic, non-diffractive structures exhibit artificial birefringence and can be engineered to serve as a half-wave plate[52], satisfying our first design requirement. We can also easily turn NWs into photodetectors by electrically contacting both ends and they have already been implemented to selectively detect light

DISTRIBUTION A: Distribution approved for public release.

of specific wavelengths, linear polarizations, and incident angles[9,26]. Without modification, linear NW-arrays exhibit identical optical responses for both CPs. However, the introduction of a series of localized displacements in the NWs (see Fig. 6a,b) renders the metasurface planar chiral and produces distinct optical responses for RCP and LCP light. These displacements are reminiscent of the atomic displacements that occur near a dislocation core in a real crystal[53] and for this reason we term the structure a dislocated NW metasurface. Whereas the architecture of a metamaterial crystal is typically linked to its optical properties, recent work has also demonstrated the powerful benefits of controllably introducing defects and disorder to achieve new properties not seen in perfect crystals[54–59]. In engineered metamaterials, the ability to continuously tune the geometry and size of defects can afford profound new insights into the evolution of certain physical properties with varying defect parameters. In turn, such fine-tuning allows one to reach fundamental performance limits. Here, we follow this approach for our dislocated NW metasurfaces.

We employ a scattered field formalism to show how the introduction of dislocations can have a dramatic impact on the optical properties of the metasurface. Our analysis indicates that the dislocations can serve as secondary localized sources of scattered field that control the coupling of free-space light waves to quasi-guided, nonlocal modes supported by the NW array. At the elementary level, this point is illustrated in Fig. 7a for a single, dislocated, 50-nm-thick Si NW illuminated by transverse-magnetic (TM) incident light, where the electric field is directed along to the NW axis. The incident electric field drives an oscillating displacement current *D* (dark-blue arrows) along the semi-infinite NW (*x*-direction). The introduction of a kink in the NW results in discontinuities in the permittivity and accumulation of positive and negative surface charges at the newly-created corners. The surface charge distributions for this very thin NW form a localized electric dipole that is oriented perpendicular to the incident electric field. This dipole orientation allows effective radiation into the guided modes of both semi-infinite NWs.

Next, we aim to create dislocations capable of selectively coupling CPL of one desired handedness. We show a conceptually intuitive strategy that builds on the observation that CPL is comprised of two orthogonally-polarized light waves for which the electric fields are oscillating with a $\pm\pi/2$ phase shift. If the dislocations can enable the coupling of both the incident TM and the orthogonal, transverse-electric (TE) polarizations to the same guided mode of the NW, we can control the excitation efficiency of the guided mode resonance by manipulating their optical interference. Constructive/destructive interference and a concomitant high/low excitation efficiency can result depending on the relative phase of the two excited waves. Dislocations in larger NW sizes can accomplish this as they can produce a variety of higher-order multipolar sources of scattered fields. Through the scattered field formalism, we can identify the nature of the multipolar sources as it naturally connects the oscillating charge distributions at the dislocations to the excited resonances in the NWs[60]. For example, the illumination of a dislocated 180-nm-thick NW with 800 nm light gives rise to the formation of an electric quadrupole for TM-polarized illumination (Fig. 7b) and a magnetic dipole for TE polarization (Fig. 7c). The electric quadrupole, induced for TM polarization, can be considered as a set of electric dipoles oriented antiparallel in the horizontal and vertical directions (as illustrated in Fig. 7b). As they are placed off the NW axes on both sides, these anti-parallel pairs can radiate into the semi-infinite NWs with the same parity as a magnetic dipole. For TE polarization, similarly to the electric dipole induced in a thin Si NW (Fig. 7a), the magnetic dipole is oriented perpendicular to the incident magnetic field. This polarization conversion is a key ingredient for our strategy as it allows effective coupling into the same guided mode for the two orthogonal polarizations of the incident light. As a result, the excitation for one handedness can be selectively enhanced through constructive interference, which occurs when these different excitation processes compensate for the $\pi/2$ phase shift between the TM- and TE-polarized components. Due to the anisotropic shape of NWs, this can simply be achieved by placing the optical resonances for these two polarizations at different spectral locations.

DISTRIBUTION A: Distribution approved for public release.

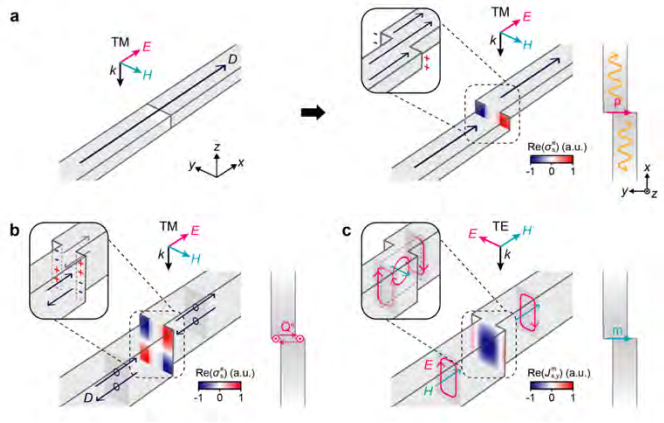

Fig. 7. Light scattering from a dislocation in single Si NW. a, Schematic of a thin Si NW (left) and a dislocated Si NW (right, δ = 40 nm) for TM polarization (h = 50 nm, w = 100 nm). Simulated surface electric charge density distribution (λ = 800 nm) is overlaid on the interface between two semi-infinite NWs (right), serving as a localized electric dipole p that radiates back into the guided modes of each semi-infinite NW. b, c, Schematic of a dislocated Si NW with a larger height (h = 180 nm, w = 100 nm, δ = 40 nm) for TM (b) and TE (c) polarizations. Simulated surface electric charge density distribution (b, λ = 800 nm) and surface magnetic current density distribution (c, λ = 800 nm) are overlaid on the interface between two semi-infinite NWs, serving as a localized electric quadrupole Q^e (represented by a set of electric dipoles oriented anti-parallel in the horizontal and vertical directions, b) and a localized magnetic dipole m (c), respectively. In a-c, the phases of incident fields are differently chosen to clarify induced different multipolar sources of scattered field.

With all of the relevant design concepts in place, we are now in a position to use optical simulations to identify an optimal design for operation at the preselected wavelength of 800 nm, as schematically shown in Fig. 8a. We start by considering a Si NW array without dislocations, i.e. with a displacement δ = 0 nm, to optimize the direct transmission pathway for the light. Using the finite element technique, we identify NW periods Λ_y, heights h, and widths w for which the array serves as a half-wave plate, requiring a π phase shift between transmitted TM- and TE-polarized light. Whereas multiple geometries meet this basic requirement, we identify that a subwavelength period Λ_y = 500 nm offers easy-to-fabricate solutions and a high transmittance. Figure 8b shows the transmittance for different NW heights and widths together with a shaded region that highlights the set of solutions for which the phase shift between TM- and TE-polarized light is close to the desired value of π. Among these solutions, we choose the dimensions for the NWs as h = 185 nm and w = 95 nm (white dot in Fig. 8b) and we use these throughout this work for the Si NW arrays suspended in free space (Figs. 8c,d and 9).

DISTRIBUTION A: Distribution approved for public release.

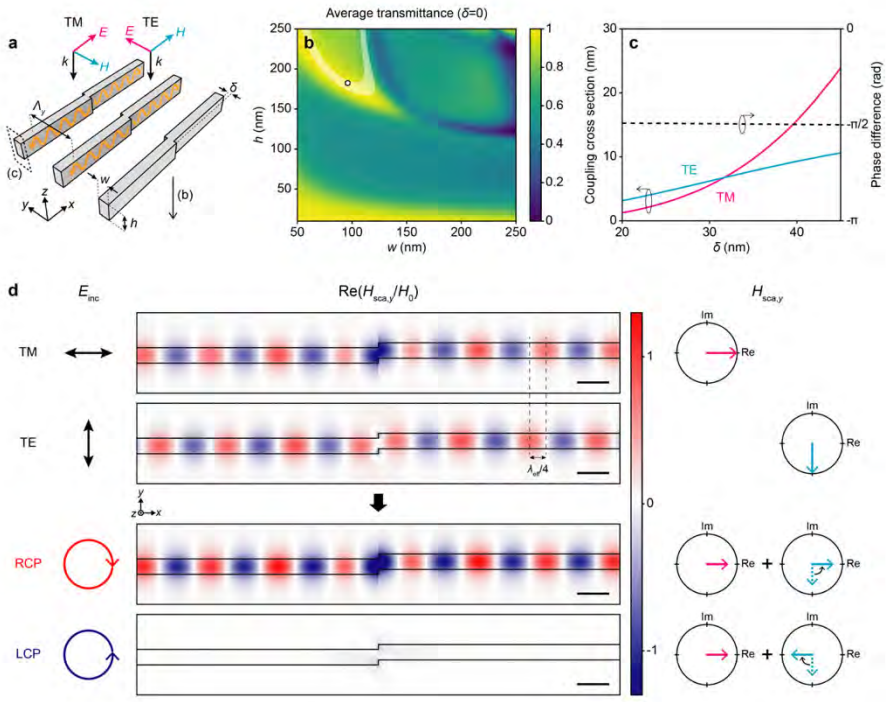

Fig. 8. Polarization-controlled excitation of guided waves at single dislocation. a, Schematic of a single dislocation introduced into a Si NW array (Λ_y = 500 nm). For LPs, excited guided waves are examined at a position away from the dislocation (indicated by the black dashed box). **b**, Simulated average transmittance (λ = 800 nm) of a non-dislocated Si NW array (δ = 0) for LP illumination. The highlighted band indicates the set of the geometries which provide the desired π phase shift (in a range of ±0.05π) between TM- and TE-polarized light in transmission. The white dot indicates the dimensions for the NWs used in **c** (h = 185 nm, w = 95 nm). **c**, Simulated coupling cross sections (solid) and phase difference (dashed) of the fundamental guided mode (λ = 800 nm) excited for TM and TE polarizations as a function of δ ($\neq$ 0). The coupling cross sections for LPs are identical around δ = 30 nm. **d**, Normalized scattered magnetic field distributions and their phasor representations (λ = 800 nm) for different incident polarizations. The phasor representations are broken down into contributions from TM- (magenta) and TE- (cyan) polarized incident fields to illustrate interference between them. Scale bar, 200 nm.

Next, we introduce a single dislocation in the NWs placed in an array and show how its geometrical properties can be designed to effectively couple both TM- and TE-polarized light to the same fundamental guided Bloch mode of the NW array (see Fig. 9b for the dispersion relation and the field distributions of the fundamental mode). Figure 8c shows how the amplitude and relative phase of the excited mode varies with the size of the dislocation for TM and TE polarizations. The amplitudes display a notable dependence on δ for both polarizations. Because each polarization induces distinct localized sources at the dislocation, it is not surprising that the coupling cross sections for TM and TE polarizations vary differently with δ. This allows us to find a certain value of δ ($\neq$ 0) where the amplitudes of the excited mode are identical for both polarizations. On the other hand, the relative phase of the excited waves is independent of δ and equal to -π/2 regardless of δ. This phase difference is strongly linked to the direct transmission properties of a Si NW array. From the coupled-mode theory, it follows that the phase difference must be ±π/2 when a Si NW array serves as a half-wave plate in the direct transmission. In the scattered field description, this phase difference results from the relative phase of the total fields inside the semi-infinite NWs for the TM and TE polarizations. To produce a π phase shift in the direct transmission, the Si NW array operates near a Fabry-Pérot resonance for TM polarization and off-resonance for TE polarization. This gives rise to the π/2 phase difference of the total fields inside the NWs for TM and TE

DISTRIBUTION A: Distribution approved for public release.

polarizations, which is directly translated to the scattered fields by their induced sources at the dislocation.

Figure 8d shows the scattered field distributions of the single dislocation for different incident polarizations. From the scattered fields for TM and TE polarization, we can see that the fundamental guided mode is launched from the dislocation and propagates along the semi-infinite Si NW array in both directions. As the dislocation size (δ = 30 nm) is chosen to give rise to the same excitation amplitude for linear polarizations (LPs), the excited guided waves for TM and TE polarizations display the same magnitude, but a quarter effective wavelength delay between them dictated by the nanoscale geometry. When RCP (or LCP) is illuminated, both TM and TE polarization components contribute simultaneously to the excitation of the guided wave. Note that the incident CP provides additional $+\pi/2$ (or $-\pi/2$) phase delay between the excitation by the two LP components. Combined, the phase delay resulting from the nanostructure design and the CP excitation leads to constructive (or destructive) interference between the excited waves by TM and TE polarizations (Fig. 8d). Therefore, only incident light for RCP can excite the fundamental guided mode in the dislocated Si NW array. The phasor representation for the scattered fields is also shown for each incident polarization.

A single, subwavelength dislocation only couples a small fraction of the incident light at one very specific location. By periodically arranging dislocations in the Si NW array along the NW length, we can resonantly enhance the polarization-controlled excitation of the quasi-guided wave (Fig. 9a). For an incident RCP plane wave, the fundamental mode is excited at each dislocation and quasi-guided waves are launched along the Si NW array (see Fig. 8c). When the period Λ_x between the dislocations is chosen to be close to the effective wavelength of the fundamental mode, the quasi-guided waves excited at each dislocation interfere constructively with each other, to build up a collective resonance (guided mode resonance). The Q of such a resonance is limited by the materials absorption and the amount of scattered light into free-space radiation at the dislocations. Given the weak material loss and small size of the dislocations, we can achieve a high-Q resonance[61–64]. The period needed to achieve a guided-mode resonance at the chosen operation wavelength of 800 nm can be approximately obtained from the simulated dispersion relation for the guided mode (Fig. 9b). The resonance strongly enhances the RCP light absorption while incident light for LCP presents only weak, non-resonant absorption (Fig. 9c). To maximize the resonant absorption from the guided-mode resonance, we can carefully adjust the radiative and absorption decay rates of the resonance to balance them. This is possible by exploring different combinations of NW heights and widths in the highlighted region in Fig. 8b. For each combination of h and w, the other dimensions, δ and Λ_x, are determined accordingly as described above (Λ_y is fixed). This procedure enables us to achieve critical coupling for the dislocated Si NW array and a CD close to the theoretical limit of 0.5 (Supplementary Note 5). Note that the maximum value of CD is slightly smaller than the theoretical limit due to the non-resonant absorption. This procedure led us to choose the NW dimensions above (h = 185 nm, w = 95 nm).

Figure 9d and 9e show the simulated transmission and reflection spectra of the periodically dislocated Si NW array for RCP and LCP, respectively. The spectra for LCP display a high transmittance and low absorptance over a broad spectral range, with a slow overall variation that results from a spectrally broad Fabry-Pérot resonance supported by the nanostructured film/NW array. On the other hand, the spectra for RCP exhibit not only the broad Fabry-Pérot resonance, but also the spectrally-narrow guided-mode resonance which leads to strong resonant absorption. As these resonances are spectrally overlapped, the scattered light through the guided-mode resonance interferes with the transmitted light through the Fabry-Pérot resonance, which gives rise to a large spectrally narrow variation in both the transmission and reflection spectra for RCP. On the guided-mode resonance, both the total transmittance and reflectance become ~0.25 and allow us to achieve an absorptance of ~0.5.

DISTRIBUTION A: Distribution approved for public release.

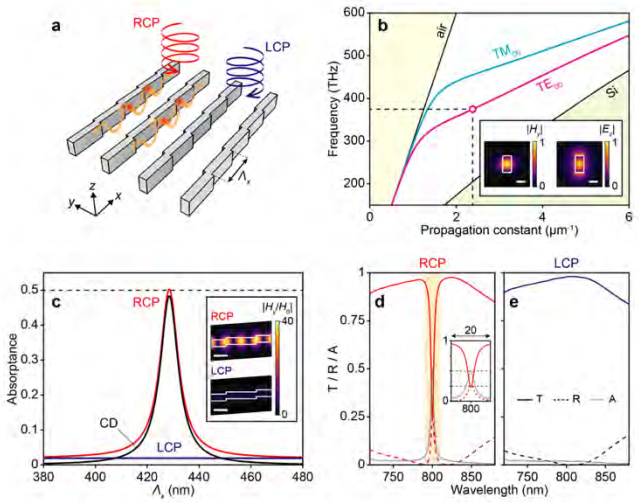

Fig. 9. Resonantly enhanced absorption using guided-mode resonance. a, Schematic of periodic dislocations introduced into the Si NW array designed in Fig. 3. At each dislocation, the fundamental guided mode is excited for RCP (Fig. 3d) and quasi-guided waves are launched along the Si NW array. b, Simulated dispersion relations for the first two guided Bloch modes of the non-dislocated Si NW array. The white dot indicates the fundamental guided mode at λ = 800 nm. The black lines indicate the light lines in air and Si, respectively. Inset: Magnetic (left) and electric (right) field distributions of the guided mode at the point indicated in the dispersion relation. Scale bar, 100 nm. c, Simulated absorptance (λ = 800 nm) for RCP (red) and LCP (blue), and corresponding CD (black) as a function of Λ_x. Inset: Normalized magnetic field distributions for RCP (top) and LCP (bottom) at the absorption peak (Λ_x = 430 nm). Scale bar, 200 nm. **d**, **e**, Simulated transmittance (T, solid), reflectance (R, dashed) and absorptance (A, grey) spectra (Λ_x = 430 nm) for RCP (red, **d**) and LCP (blue, **e**). Inset: Optical spectra for RCP near the resonance wavelength (over the shaded range). The black dashed lines indicate 0.25 and 0.5, respectively.

To experimentally demonstrate a CD photodetector, we fabricate a periodically dislocated Si NW array on a transparent sapphire substrate (Fig. 10a). We slightly redesign the geometry of the dislocated Si NW array (Λ_x = 370 nm, Λ_y = 430 nm, h = 320 nm, w = 65 nm, δ = 35 nm) to take into account the presence of the substrate. For photocurrent extraction, we fabricate aluminum ohmic contacts at the ends of the dislocated Si NW array (43 × 37 μm^2). Next, we first characterize the optical absorption of the fabricated CD photodetector (Fig. 10b). From transmission and reflection measurements, we calculate the absorptance by subtracting the transmittance and reflectance from unity. In the experimental absorption spectra, the dislocated Si NW array exhibits a high-Q optical resonance for RCP light only. The sensitivity of the resonance to the handedness of the light results in a significant CD on resonance, corroborating the selective modal excitation described above. The greyed out areas in the optical spectra correspond to the spectral range in which first-order diffraction channels open up in the transparent sapphire substrate. As the diffracted light is not captured in the measurements, the calculated absorptance is higher than the actual amount in this spectral range. With an applied external bias, we also characterize the photocurrent response of the CD photodetector (Fig. 10c). For both RCP and LCP, the measured external quantum efficiency (EQE) spectra are consistent with the experimental optical absorption spectra. A resonantly enhanced EQE for RCP light over LCP light is observed and we can use this to directly distinguish between these polarization states. Note that the spectral broadening of the EQE spectra as compared to the absorption spectra can be attributed to a spatially-dependent charge collection efficiency. We also experimentally demonstrate a CD photodetector with resonant absorption and EQE for LCP by simply reversing the direction of the displacements for each of the dislocations.

DISTRIBUTION A: Distribution approved for public release.

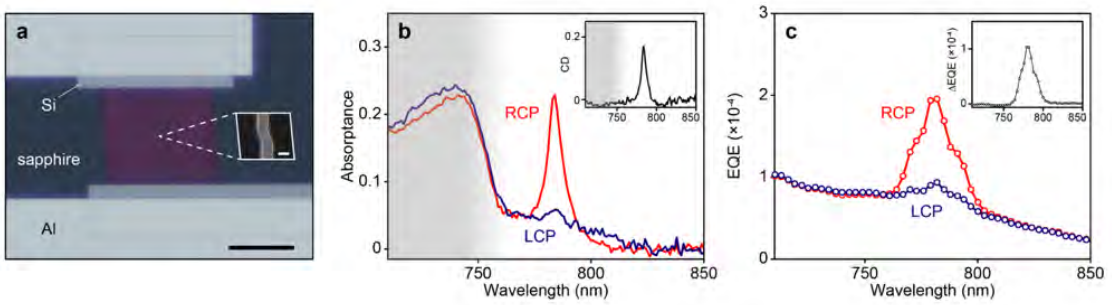

Fig. 10. Experimental demonstration of a CD photodetector. a, Reflected optical micrograph of the fabricated CD photodetector under white-light illumination. Scale bar, 25 μm. Inset: SEM of a unit cell of the fabricated Si nanostructures. Scale bar, 50 nm. **b**, Measured optical absorption spectra for RCP (red) and LCP (blue). Inset: Measured CD spectrum. The greyed out areas in optical spectra indicate the spectral range in which first-order diffraction channels open up in the transparent substrate. **c**, Measured EQE spectra for RCP (red) and LCP (blue). Inset: Measured differential EQE spectrum.

In conclusion, we demonstrate the use of a nonlocal semiconductor metasurface to build an integrated photodetector for circularly-polarized light. Using a dislocation as a building block, we are able to systematically design a Si metasurface that displays a guided-mode resonance only for a circular polarization of interest. The engineering of the resonance allows us to reach the theoretical maximum of CD in a symmetric external environment. We experimentally implement the metasurface in a CD photodetector and verify the key physics behind its operation using optical absorption and photocurrent measurements. These dislocated nanostructures can be employed in a range of applications for polarimetric sensing and imaging where dense integration is required. This work was published in the journal Optica.[65] Similar high-Q designs were used in a joint project with the Dionne group at Stanford to steer light across a very narrow spectral bandwidth. That work was published in Nature Nanotechnology.[66]

II.4 References

1. Kildishev, Alexander V. Boltasseva, A. & Shalaev, V. M. Planar Photonics with Metasurfaces. *Science* **339**, 1232009 (2013).
2. Kuznetsov, A. I., Miroshnichenko, A. E., Brongersma, M. L., Kivshar, Y. S. & Luk'yanchuk, B. Optically resonant dielectric nanostructures. *Science* **354**, (2016).
3. Cao, L., Fan, P., Barnard, E. S., Brown, A. M. & Brongersma, M. L. Tuning the color of silicon nanostructures. *Nano Lett.* **10**, 2649–2654 (2010).
4. Cao, L., Fan, P. & Brongersma, M. L. Optical coupling of deep-subwavelength semiconductor nanowires. *Nano Lett.* **11**, (2011).
5. Prodan, E., Radloff, C., Halas, N. J. & Nordlander, P. A hybridization model for the plasmon response of complex nanostructures. *Science* **302**, 419–422 (2003).
6. Nordlander, P., Oubre, C., Prodan, E., Li, K. & Stockman, M. I. Plasmon Hybridization in Nanoparticle Dimers. *Nano Lett.* **4**, 899–903 (2004).
7. Cao, L., Fan, P. & Brongersma, M. L. Optical Coupling of Deep-Subwavelength Semiconductor Nanowires. *Nano Lett.* **11**, 1463–1468 (2011).
8. Haynes, C. L. *et al.* Nanoparticle optics: The importance of radiative dipole coupling in two-dimensional nanoparticle arrays. *J. Phys. Chem. B* **107**, 7337–7342 (2003).

DISTRIBUTION A: Distribution approved for public release.

9. Yi, S. *et al.* Subwavelength angle-sensing photodetectors inspired by directional hearing in small animals. *Nat. Nanotechnol.* **13**, 1143–1147 (2018).
10. Lalanne, P., Yan, W., Vynck, K., Sauvan, C. & Hugonin, J. P. Light Interaction with Photonic and Plasmonic Resonances. *Laser Photonics Rev.* **12**, 1700113 (2018).
11. Li, Q., Wu, T., van de Groep, J., Lalanne, P. & Brongersma, M. Structural color from a coupled nanowire pair beyond the bonding and anti-bonding model. *Optica* **8**, 464–470 (2021).
12. Song, J. H. *et al.* Nanoelectromechanical modulation of a strongly-coupled plasmonic dimer. *Nature Communications* **12**, 48 (2021).
13. Song, J. H. *et al.* Nanoelectromechanical modulation of a strongly-coupled plasmonic dimer. *Nat. Commun.* **12**, 1–7 (2021).
14. Shaltout, A. M., Shalaev, V. M. & Brongersma, M. L. Spatiotemporal light control with active metasurfaces. *Science* **364**, 374–377 (2019).
15. Bomzon, Z., Biener, G., Kleiner, V. & Hasman, E. Spatial Fourier-transform polarimetry using space-variant subwavelength metal-stripe polarizers. *Opt. Lett.* **26**, 1711–1713 (2001).
16. Pors, A., Nielsen, M. G. & Bozhevolnyi, S. I. Plasmonic metagratings for simultaneous determination of Stokes parameters. *Optica* **2**, 716–723 (2015).
17. Balthasar Mueller, J. P., Leosson, K. & Capasso, F. Ultracompact metasurface in-line polarimeter. *Optica* **3**, 42–47 (2016).
18. Basiri, A. *et al.* Nature-inspired chiral metasurfaces for circular polarization detection and full-Stokes polarimetric measurements. *Light Sci. Appl.* **8**, 78 (2019).
19. Yokogawa, S., Burgos, S. P. & Atwater, H. A. Plasmonic color filters for CMOS image sensor applications. *Nano Lett.* **12**, 4349–4354 (2012).
20. Brongersma, M. L. Plasmonic Photodetectors, Photovoltaics, and Hot-Electron Devices. *Proc. IEEE* **104**, 2349–2361 (2016).
21. McClung, A., Samudrala, S., Torfeh, M., Mansouree, M. & Arbabi, A. Snapshot spectral imaging with parallel metasystems. *Sci. Adv.* **6**, eabc7646 (2020).
22. Benetou, M. I., Thomsen, B. C., Bayvel, P., Dickson, W. & Zayats, A. V. Four-level polarization discriminator based on a surface plasmon polaritonic crystal. *Appl. Phys. Lett.* **98**, 43–46 (2011).
23. Park, H. *et al.* Filter-free image sensor pixels comprising silicon nanowires with selective color absorption. *Nano Lett.* **14**, 1804–9 (2014).
24. Li, Q., van de Groep, J., Wang, Y., Kik, P. G. & Brongersma, M. L. Transparent multispectral photodetectors mimicking the human visual system. *Nat. Commun.* **10**, 1–8 (2019).
25. Bohren, F. & Huffman, D. *Absorption and Scattering of Light by Small Particles*. (Wiley, 1983).
26. Cao, L. *et al.* Engineering light absorption in semiconductor nanowire devices. *Nat. Mater.* **8**, 643–647 (2009).
27. Afshinmanesh, F., White, J. S., Cai, W. & Brongersma, M. L. Measurement of the polarization state of light using an integrated plasmonic polarimeter. *Nanophotonics* **1**, 125–129 (2012).
28. Chiou, T. H. *et al.* Circular Polarization Vision in a Stomatopod Crustacean. *Curr. Biol.* **18**, 429–434 (2008).

DISTRIBUTION A: Distribution approved for public release.

29. Sherson, J. F. *et al.* Quantum teleportation between light and matter. *Nature* **443**, 557–560 (2006).
30. Farshchi, R., Ramsteiner, M., Herfort, J., Tahraoui, A. & Grahn, H. T. Optical communication of spin information between light emitting diodes. *Appl. Phys. Lett.* **98**, 162508 (2011).
31. Brooks, W. H., Guida, W. C. & Daniel, K. G. The Significance of Chirality in Drug Design and Development HHS Public Access. *Curr Top Med Chem* **11**, 760–770 (2011).
32. Talmage, D. A. & Curran, P. J. Remote sensing using partially polarized light. *Int. J. Remote Sens.* **7**, 47–64 (1986).
33. Maguid, E. *et al.* Photonic spin-controlled multifunctional shared-aperture antenna array. *Science* **352**, 1202–1206 (2016).
34. Rubin, N. A. *et al.* Matrix Fourier optics enables a compact full-Stokes polarization camera. *Science (80-.).* **364**, (2019).
35. Schaibley, J. R. *et al.* Valleytronics in 2D materials. *Nat. Rev. Mater.* **1**, (2016).
36. Lu, L., Joannopoulos, J. D. & Soljačić, M. Topological photonics. *Nat. Photonics* **8**, 821–829 (2014).
37. Yang, Y., Da Costa, R. C., Fuchter, M. J. & Campbell, A. J. Circularly polarized light detection by a chiral organic semiconductor transistor. *Nat. Photonics* **7**, 634–638 (2013).
38. Chen, C. *et al.* Circularly polarized light detection using chiral hybrid perovskite. *Nat. Commun.* **10**, 1–7 (2019).
39. Ishii, A. & Miyasaka, T. Direct detection of circular polarized light in helical 1D perovskite-based photodiode. *Sci. Adv.* **6**, eabd3274 (2020).
40. Li, W. *et al.* Circularly polarized light detection with hot electrons in chiral plasmonic metamaterials. *Nat. Commun.* **6**, 1–7 (2015).
41. Hentschel, M., Schäferling, M., Duan, X., Giessen, H. & Liu, N. Chiral plasmonics. *Sci. Adv.* **3**, 1–13 (2017).
42. Gansel, J. K. *et al.* Gold helix photonic metamaterial as broadband circular polarizer. *Science* **325**, 1513–1515 (2009).
43. Zhao, Y., Belkin, M. a. & Alù, A. Twisted optical metamaterials for planarized ultrathin broadband circular polarizers. *Nat. Commun.* **3**, 870 (2012).
44. Lin, J. *et al.* Polarization-controlled tunable directional coupling of surface plasmon polaritons. *Science* **340**, 331–334 (2013).
45. Haus, H. A. *Waves and fields in optoelectronics*. (Prentice-Hall, 1984).
46. Fan, S., Suh, W. & Joannopoulos, J. D. Temporal coupled-mode theory for the Fano resonance in optical resonators. *J. Opt. Soc. Am. A* **20**, 569 (2003).
47. Woltersdorff, W. Über die optischen Konstanten dünner Metallschichten im langwelligen Ultrarot. *Zeitschrift für Phys.* **91**, 230–252 (1934).
48. Yin, X. *et al.* Beam switching and bifocal zoom lensing using active plasmonic metasurfaces. *Light Sci. Appl.* **6**, e17016–e17016 (2017).
49. Yin, X., Schäferling, M., Metzger, B. & Giessen, H. Interpreting chiral nanophotonic spectra: The plasmonic Born-Kuhn model. *Nano Lett.* **13**, 6238–6243 (2013).
50. Papakostas, A. *et al.* Optical Manifestations of Planar Chirality. *Phys. Rev. Lett.* **90**, 107404 (2003).

DISTRIBUTION A: Distribution approved for public release.

51. Valev, V. K., Baumberg, J. J., Sibilia, C. & Verbiest, T. Chirality and chiroptical effects in plasmonic nanostructures: Fundamentals, recent progress, and outlook. *Adv. Mater.* **25**, 2517–2534 (2013).
52. Lin, D., Fan, P., Hasman, E. & Brongersma, M. L. Dielectric gradient metasurface optical elements. *Science* **345**, 298–302 (2014).
53. Theoretical, P. I., By, G. I. T. & Yarrow, R. S. The mechanism of plastic deformation of crystals. Part I.—Theoretical. *Proc. R. Soc. London. Ser. A, Contain. Pap. a Math. Phys. Character* **145**, 362–387 (1934).
54. Gorsky, S. *et al.* Directional light emission enhancement from LED-phosphor converters using dielectric Vogel spiral arrays. *APL Photonics* **126103**, 126103 (2019).
55. Meeussen, A. S., Oğuz, E. C., Shokef, Y. & Hecke, M. van. Topological defects produce exotic mechanics in complex metamaterials. *Nat. Phys.* **16**, 307–311 (2020).
56. Baraclough, M., Hooper, I. R. & Barnes, W. L. Direct observation of defect modes in molecular aggregate analogs. *Phys. Rev. B* **102**, 1–6 (2020).
57. Nguyen, V. C., Chen, L. & Halterman, K. Total transmission and total reflection by zero index metamaterials with defects. *Phys. Rev. Lett.* **105**, 1–4 (2010).
58. Maguid, E. *et al.* Disorder-induced optical transition from spin Hall to random Rashba effect. *Science (80-.).* **358**, 1411–1415 (2017).
59. Yannai, M. *et al.* Order and Disorder Embedded in a Spectrally Interleaved Metasurface. *ACS Photonics* **5**, 4764–4768 (2018).
60. Kuznetsov, A. I., Miroshnichenko, A. E., Brongersma, M. L., Kivshar, Y. S. & Lukyanchuk, B. Optically resonant dielectric nanostructures. *Science* **354**, 2472–2472 (2016).
61. Quaranta, G., Basset, G., Martin, O. J. F. & Gallinet, B. Recent Advances in Resonant Waveguide Gratings. *Laser Photonics Rev.* **12**, 1–31 (2018).
62. Magnusson, R. & Wang, S. S. New principle for optical filters. *Appl. Phys. Lett.* **61**, 1022 (1992).
63. Liu, H. & Lalanne, P. Microscopic theory of the extraordinary optical transmission. *Nature* **452**, 728–731 (2008).
64. Fano, U. The Theory of Anomalous Diffraction Gratings and of Quasi-Stationary Waves on Metallic Surfaces (Sommerfeld's Waves). *J. Opt. Soc. Am.* **31**, 213 (1941).
65. Hong, J. *et al.* Nonlocal metasurface for circularly polarized light detection. *Optica* **10**, 134–141 (2023).
66. Lawrence, M. *et al.* High quality factor phase gradient metasurfaces. *Nat. Nanotechnol.* **15**, 956–961 (2020).
67. Gigli, C. *et al.* Fundamental Limitations of Huygens' Metasurfaces for Optical Beam Shaping. *Laser Photonics Rev.* **15**, 2000448 (2021).

DISTRIBUTION A: Distribution approved for public release.

III. Personnel and Training Opportunities

III. 1. Personnel Supported

At Stanford University, this program supported research in the group of Prof. Mark L. Brongersma (PI). At different times, it funded work by a students Qitong Li and Jiho Hong. It also funded work by a postdoc Jung-Hwan Song. The researchers were together working on several projects aimed at the development of metamaterial dynamic and spectrally selective building blocks and devices.

III.2. Research Training of Students

The training of graduate students and postdoctoral researchers was a critical aspect of this project. The sudden burst of activity in the field of metasurface and metafilms has led to hundreds of publications in the international literature and popular press. New conferences and symposia are devoted to just this topic (a number organized by the PIs). Major companies, such as Northrop Grumman, Samsung, Intel, META/Facebook, Google, Corning, and Hewlett Packard now have active research efforts in this field of study.

IV. Dissemination of Research findings

IV.1.Publications, Books, and Presentations

The research from this program led to a total of 7 publications in refereed journals and one that is currently under review. The PI also gave more than 15 invited talks (including several keynotes) each year on the topics related to this program. He also incorporated the material from this program into a short courses taught at the CLEO conference every year on plasmonics and nanophotonics. The students funded by this effort presented a number of contributed talks at International conferences.

Publications

1) Shaltout, A. M., Shalaev, V. M. & Brongersma, M. L. Spatiotemporal light control with active metasurfaces. Science 364, 374–377 (2019).
2) Lawrence, M. et al. High quality factor phase gradient metasurfaces. Nat. Nanotechnol. 15, 956–961 (2020).12.
3) Song, J. H. et al. Nanoelectromechanical modulation of a strongly-coupled plasmonic dimer. Nature Communications 12, 48 (2021).
4) Song, J. H. et al. Nanoelectromechanical modulation of a strongly-coupled plasmonic dimer. Nat. Commun. 12, 1–7 (2021).
5) Brongersma, M. L. The road to atomically thin metasurface optics. *Nanophotonics* **10**, 643–654 (2021).
6) Gigli, C. et al. Fundamental Limitations of Huygens' Metasurfaces for Optical Beam Shaping. Laser Photonics Rev. 15, 2000448 (2021).
7) Hong, J. et al. Nonlocal metasurface for circularly polarized light detection. Optica 10, 134–141 (2023).

IV.2. Interactions and Transitions

This project has created a number of exciting opportunities for knowledge transfer. The work on integrated detectors has attracted the attention of several companies, including Northrop Grumman and Metamaterials Technology Incorporated. This could also impact

DISTRIBUTION A: Distribution approved for public release.

the MURI program on metasurfaces for optical imaging that is led by Professor Maiken Mikkelsen. Knowledge transfer also occurred via individual interactions, presentations, and short courses.

IV.3. Honors and Awards

Brongersma received a variety of scientific honors. The most notable recent honors are:

- Highly Cited Researcher 2018 – Pres. (Clarivate Analytics)
- Fellow of Materials Research Society (MRS), 2023
- Honorary Doctorate University of Southern Denmark, 2022
- Stephen Harris Professor of the School of Engineering, 2020
- Director-at-large of the Optical Society Board of Directors, Elected (2017 - 2019)
- Symposium Chair Nanoscience + Engineering event at SPIE Annual Meeting (2019)

DISTRIBUTION A: Distribution approved for public release.